30. J. Takekawa, H. Mikada, T. Goto, *Nat. Hazards Earth Syst. Sci.* **13**, 231–237 (2013).
31. F. Tajima, H. Kanamori, *Geophys. Res. Lett.* **12**, 345–348 (1985).
32. H. Kanamori, *Annu. Rev. Earth Planet. Sci.* **14**, 293–322 (1986).
33. M. Simons *et al.*, *Science* **332**, 1421–1425 (2011).
34. D. Zhao, Z. Huang, U. Umino, A. Hasegawa, H. Kanamori, *Geophys. Res. Lett.* **38**, L17308 (2011).
35. F. Tajima, B. L. N. Kennett, *Geophys. Res. Lett.* **39**, L05307 (2012).

ACKNOWLEDGMENTS

We thank K. Sado, S. Takahashi, S. Hirata, and K. Osono for assistance in the field; M. Miyawaki for discussions during this study; and B. Di and N. Akiyama for help in arranging the field work and processing the images. We acknowledge the Disaster Information Laboratory (DIL), National Research Institute for Earth Science and Disaster Resilience for kindly providing seismic data. The raw data for focal mechanisms, foreshocks, and aftershocks are available directly from DIL. This work was partially supported by a Science Project (no. 15K01248) of the Ministry of Education, Culture, Sports, Science and Technology of Japan.

SUPPLEMENTARY MATERIALS

www.sciencemag.org/content/354/6314/869/suppl/DC1
Figs. S1 to S6

30 June 2016; accepted 7 October 2016
Published online 20 October 2016
10.1126/science.aah4629

NANOMATERIALS

Single-particle mapping of nonequilibrium nanocrystal transformations

Xingchen Ye,[1]* Matthew R. Jones,[1]* Layne B. Frechette,[1] Qian Chen,[1,2] Alexander S. Powers,[1] Peter Ercius,[7] Gabriel Dunn,[3] Grant M. Rotskoff,[5] Son C. Nguyen,[1] Vivekananda P. Adiga,[3] Alex Zettl,[3,6,8] Eran Rabani,[1,6,9] Phillip L. Geissler,[1] A. Paul Alivisatos[1,4,6,8]†

Chemists have developed mechanistic insight into numerous chemical reactions by thoroughly characterizing nonequilibrium species. Although methods to probe these processes are well established for molecules, analogous techniques for understanding intermediate structures in nanomaterials have been lacking. We monitor the shape evolution of individual anisotropic gold nanostructures as they are oxidatively etched in a graphene liquid cell with a controlled redox environment. Short-lived, nonequilibrium nanocrystals are observed, structurally analyzed, and rationalized through Monte Carlo simulations. Understanding these reaction trajectories provides important fundamental insight connecting high-energy nanocrystal morphologies to the development of kinetically stabilized surface features and demonstrates the importance of developing tools capable of probing short-lived nanoscale species at the single-particle level.

Nanoscience relies on the ability to create nonequilibrium states of matter in which metastable materials are spatially organized in close proximity to yield desired properties. As a result, much effort is currently dedicated to understanding and controlling the complex pathways of formation (*1*), transformation (*2*–*5*), and dissolution (*6*, *7*) of individual nanoscale building blocks. The majority of studies on the evolution of nanocrystal-based chemical reactions have relied on methods to isolate intermediates and characterize them by electron microscopy or probe the ensemble with spectroscopic techniques. Although these approaches have provided new fundamental knowledge, their time-resolution is severely limited and/or the ensemble averaging can obscure the details of individual pathways.

Methods for the direct imaging of the evolution of individual nanoparticle species in a liquid environment are under active development because they enable the preservation of dynamic processes present in the native colloid (*1*, *8*–*14*). Recently, our group has developed transmission electron microscopy (TEM) liquid cells based on the trapping of thin fluids between sheets of graphene (Fig. 1A) (*15*). The superior electron transparency of these windows has allowed for detailed tracking of nucleation and growth phenomena as well as atomistic reconstruction of nanocrystals (*15*, *16*).

The majority of liquid-phase electron microscopy studies of transient nanoscale phenomena have focused on beam-induced nucleation and growth processes (*1*, *9*, *10*, *15*, *17*, *18*). These studies often produce an ill-defined set of randomly oriented nanoparticles that requires atomic resolution to deduce crystallographically meaningful information about liquid-phase phenomena (*1*, *15*). If, on the other hand, one monitors the dissolution of presynthesized particles with a well-defined crystallographic habit (vis-à-vis their shape), far more information is available regarding nonequilibrium processes because the orientation, zone axis, and exposed crystal facets can be known ahead of time and can be monitored kinetically through the evolution of particle shape over time.

We use graphene liquid cell TEM to monitor in real time single-particle, nonequilibrium structural transformations of anisotropic gold nanocrystals as they undergo oxidative dissolution in their native aqueous environment (Fig. 1 and figs. S1 to S3). $FeCl_3$ is introduced as the primary oxidative etchant, the concentration of which allows for a controlled rate of etching in the presence of the electron beam, with virtually no etching in the absence of the beam (Fig. 1A). This occurs because additional oxidizing species formed as radiolysis products by the electron beam, such as OH radicals, can be used to locally trigger nanoparticle etching (figs. S4 to S9 and movie S3) (*17*, *19*). Monte

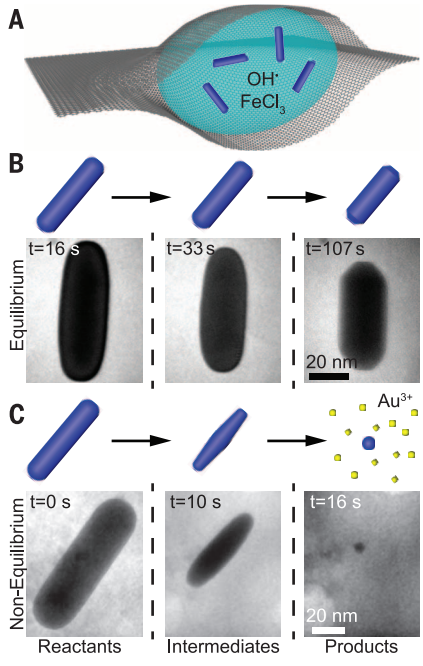

Fig. 1. Real-time observation of near-equilibrium and nonequilibrium nanocrystal species in a graphene liquid cell. (**A**) Schematic liquid cell encapsulating a solution of gold nanocrystals. (**B**) Idealized reaction pathway and TEM images extracted from movie S1 showing the reaction to generate near-equilibrium rods with flat {100} facets at the tips. (**C**) Idealized reaction pathway and TEM images extracted from movie S2 showing the transition from rods to a nonequilibrium ellipsoidal intermediate with sharp tips.

[1]Department of Chemistry, University of California, Berkeley, Berkeley, CA 94720, USA. [2]Miller Institute for Basic Research in Science, University of California, Berkeley, Berkeley, CA 94720, USA. [3]Department of Physics, University of California, Berkeley, Berkeley, CA 94720, USA. [4]Department of Materials Science and Engineering, University of California, Berkeley, Berkeley, CA 94720, USA. [5]Biophysics Graduate Group, University of California, Berkeley, Berkeley, CA 94720, USA. [6]Materials Sciences Division, Lawrence Berkeley National Laboratory, Berkeley, CA 94720, USA. [7]Molecular Foundry, Lawrence Berkeley National Laboratory, Berkeley, CA 94720, USA. [8]Kavli Energy NanoScience Institute, University of California, Berkeley, and Lawrence Berkeley National Laboratory, Berkeley, CA 94720, USA. [9]Raymond and Beverly Sackler Center for Computational Molecular and Materials Science, Tel Aviv University, Tel Aviv 69978, Israel.
*These authors contributed equally to this work. **†Corresponding author. Email: alivis@berkeley.edu**

Carlo simulations corroborate the observation of nonequilibrium nanocrystal reaction pathways and shed light on their mechanistic underpinnings.

These methods are illustrated first with a simple shape, rods (Fig. 1). At low $FeCl_3$ concentrations, reactions proceed slowly and show the development of low-energy facets (Fig. 1B and movies S1 and S4). In this scenario, the rate of etching is slow compared to the rate at which the particle is able to restructure and adopt a shape that is close to equilibrium (*20*). At high $FeCl_3$ concentrations, however, fast-reaction kinetics constantly drive the system out of equilibrium and the nanocrystal transiently adopts an ellipsoidal shape (Fig. 1C and movie S2). Previous ex situ studies have investigated the etching of gold nanorods but have primarily observed tip-selective shortening (*21*).

The distinguishing feature of the nonequilibrium rod reaction is the change in the relative proportions of the particle through the development of tips that are sharper than the diameter—i.e., the formation of ellipsoids (Fig. 2A, fig. S10, and movie S5). Analysis of the longitudinal dissolution rate and tip curvature changes over time show that periods during which the rod tips become sharper are well correlated with accelerated etching of the particle (Fig. 2B and fig. S11). To better understand the spatiotemporal details of the reaction, we constructed time-domain contour plots: cross-sectional outlines of a changing nanocrystal extracted from frames that are equally spaced in time and colored based on calculation of the in-plane local curvature (Fig. 2C and figs. S12 and S13) (*22*). These data are consistent with the expectation that, because the rod tips are curved along two orthogonal dimensions while the sides are curved along one, the tips possess a lower areal ligand density and are therefore more chemically accessible and etch faster (fig. S14) (*22*–*24*); this interpretation is supported by Monte Carlo simulations of rod etching (fig. S15 and movie S6). Whereas in the near-equilibrium case, atoms at the tips have an opportunity to relax (e.g., via surface diffusion) (fig. S16 and movie S7) (*20*, *23*), the persistent oxidative environment reacts with these species selectively, accelerating the reaction and driving the transient stabilization of the ellipsoidal intermediate. Etching reactions conducted on rods with synthetically blunted tips follow the same reaction trajectory (ellipsoidal intermediate), albeit with slower initial kinetics corresponding to selective removal of the blunt features (Fig. 2, D to F; figs. S12 and S13; and movies S8 and S9). Qualitatively similar dependencies on tip dimensionality and tip curvature are observed for other nanocrystal shapes as well as when a rod and blunted rod pair are etched in the same field of view under identical conditions (figs. S17 and S18 and movies S10 to S16).

The etching of pseudo–one-dimensional nanocrystals demonstrates that persistent and selective etching at high-energy local features drives the formation of nonequilibrium intermediate shapes. However, for this class of particles the surface faceting is not easily characterized or agreed upon in the literature (*25*); therefore, deducing a more detailed, atomistic understanding of far-from-equilibrium reactions is challenging. To address this, single-crystalline polyhedral gold nanocrystals with definitive surface faceting were subjected to the oxidative environment in the liquid cell and were observed to transition through crystallographically well-defined intermediate shapes.

We describe results for a {100}-faceted cube (movies S17 and S18). The square cross-section indicative of the ⟨100⟩ zone axis of a cube is observed to transition through a faceted intermediate before adopting an isotropic shape and being oxidized completely (Fig. 3, A and B). To determine a crystallographic assignment for the intermediate shape, the angles between candidate {hkl} crystal facets viewed along the ⟨100⟩ zone axis were calculated and compared to those measured in the TEM images (Fig. 3, C and D). This analysis reveals a transformation to high-energy {310} facets, indicative of a tetrahexahedron (THH)–shaped nanocrystal as the longest-lived intermediate (*26*, *27*).

We observe a similar shape transformation in Monte Carlo simulations of a schematic kinetic model for nanocrystal etching (Fig. 3, B and D, and movies S19 and S20). We take Au atoms to reside on sites of a face-centered cubic (fcc) lattice and adopt rate constants $k(n)$ for etching of surface-exposed atoms that depend only on their coordination number, n. Despite its simplicity, this model produces a THH intermediate for a broad range of parameter values (fig. S19). This

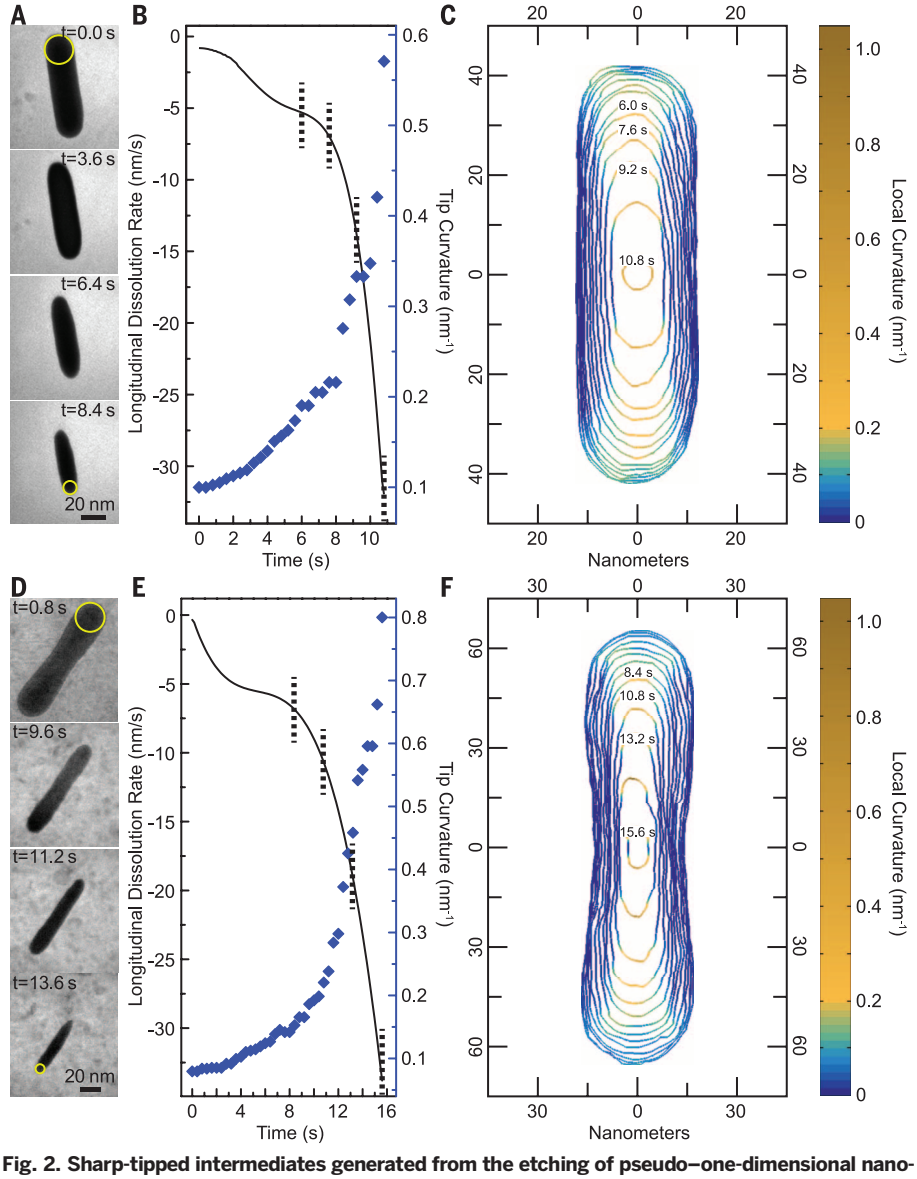

Fig. 2. Sharp-tipped intermediates generated from the etching of pseudo–one-dimensional nanocrystals. Dissolution of a gold rod (**A** to **C**) and blunted rod (**D** to **F**) under nonequilibrium conditions. Selected time-lapse TEM images extracted from movies S5 (A) and S8 (D), plots of longitudinal dissolution rate and tip curvature as a function of time [(B) and (E)], and time-domain contour plots [(C) and (F)]. Yellow circles in (A) and (D) highlight the extrema of cross-sectional tip curvature. Vertical dotted lines in (B) and (E) correspond to the time-labeled contours in (C) and (F). Contour lines are spaced in time by 0.8 s in (C) and 1.2 s in (F).

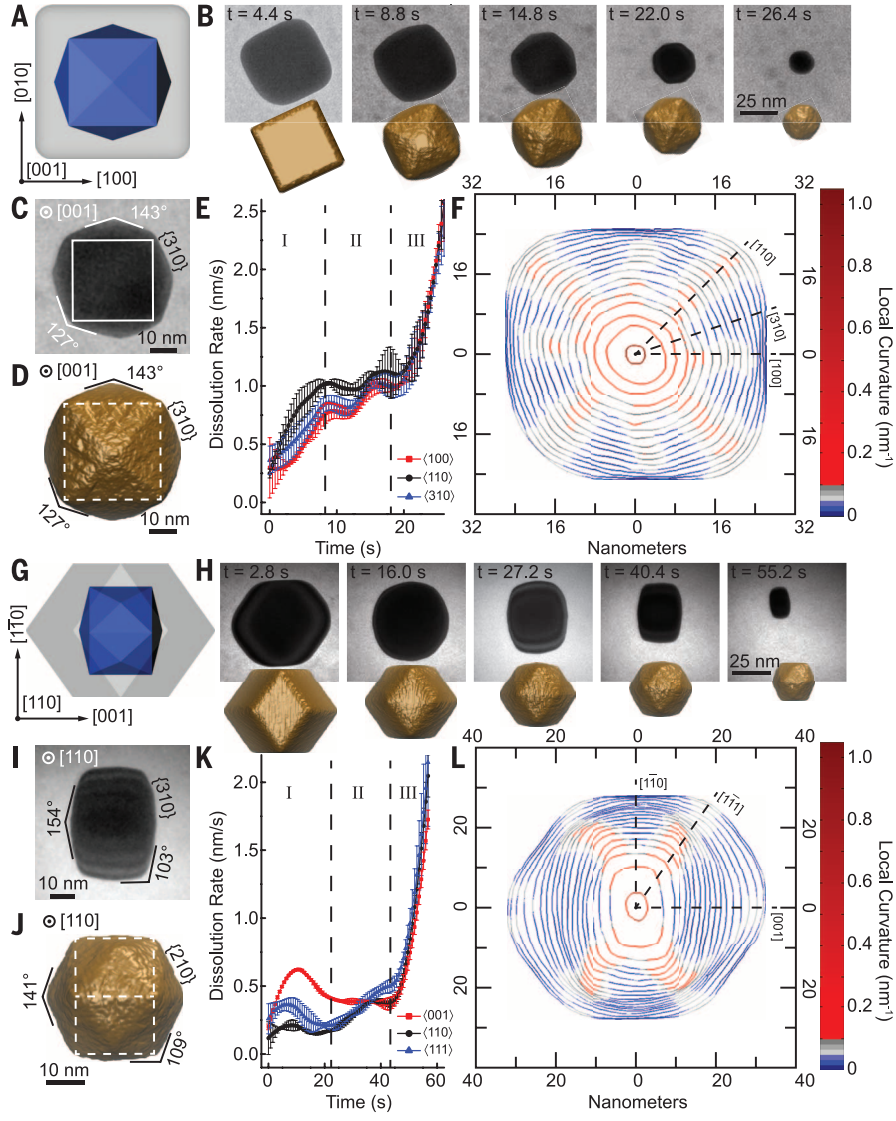

Fig. 3. Crystallographically well-defined intermediates generated from polyhedral nanocrystals. Transition of a cube (**A** to **F**) and rhombic dodecahedron (**G** to **L**) to a tetrahexahedron during nonequilibrium etching. [(A) and (G)] Model of a crystallographically oriented particle (gray) with intermediate tetrahexahedra shown internally (blue). [(B) and (H)] Time-lapse TEM images and corresponding snapshots from Monte Carlo simulations extracted from movies S17 and S19 (B) and S27 and S29 (H). Tetrahexahedron intermediates with labeled zone axis and calculated {hk0} facet angles are shown for the cube [(C) and (D)] and rhombic dodecahedron [(I) and (J)] reactions for experiment [(C) and (I)] and simulation [(D) and (J)]. [(E) and (K)] Crystallographic dissolution rates extracted from contour plots, averaged over several symmetric directions. [(F) and (L)] Time-domain contour plots with relevant crystallographic directions labeled as dotted lines. Contour lines are spaced in time by 1.6 s in (F) and (L).

nonequilibrium structure is unlikely to be a consequence of the electron beam, the particular oxidation chemistry employed in the liquid cell, or the presence of surface-bound ligands, because these effects are not explicitly considered in the simulation. When the driving force for oxidation is reduced in experiments, cubes transform into truncated octahedra (fig. S20 and movies S21 and S22) (*28*), the expected equilibrium Wulff shape for an fcc lattice (fig. S21) (*20*, *23*). This same equilibrium transformation is observed in simulations when mechanisms of surface relaxation are introduced (figs. S19 and S22 and movies S23 to S25; see supplementary materials).

Because the particles do not visibly rotate throughout the etching reaction, the crystallographic zone axis is constant and can be known beforehand by the cross-sectional appearance of the initial nanocrystals. This allows for the quantification of dissolution rates along specific [uvw] directions from time-domain contour maps (Fig. 3, E and F, and figs. S23 to S25). These data represent an experimental manifestation of the so-called kinetic Wulff construction (*23*) but provide additional insight because they allow one to extract the time dependence of crystallographic dissolution rates (Fig. 3E and fig. S26). The ⟨110⟩ edges of the cubic nanocrystal exhibit the fastest initial etching rates, revealing the {310} THH facets that then experience a period of transient metastability (region II, Fig. 3E) before all rates accelerate at small particle sizes (region III, Fig. 3, E and F).

The formation of a well-defined THH intermediate is driven primarily by a coordination number (n)–dependent etching process (see supplementary materials). When the rate of deletion of surface atoms with $n = 6$ is much slower than surface relaxation, the equilibrium truncated octahedron is observed (fig. S19 and movies S24 and S25). However, when the rate of removal of surface atoms with $n = 6$ is faster than both surface relaxation and the removal of $n \geq 7$ atoms, the nonequilibrium THH intermediate is observed (Fig. 3, B and D; fig. S19; and movies S24 and S25). This occurs through the lateral recession of sequential {100} layers via etching of the peripheral edge atoms that tend to have $n \leq 6$ (Fig. 4A, fig. S27, and movie S26). This results in the gradual transition from {100} facets on the initial cube to a series of vicinal {hk0} facets and is corroborated by measurement of the facet h-index in both experiment and simulation (Fig. 4B). Because vicinal {hk0} facets consist of a series of {100} terraces ($n = 8$) separated by steps ($n = 6$) (Fig. 4, C and D), continued removal of $n = 6$ atoms eventually results in a far-from-equilibrium condition in which a series of stepped terraces are receding via their edges at a constant rate, resulting in the transient existence of the THH intermediate (Fig. 4E). This mechanism, known as step-recession (*29*, *30*), is the reverse of the well-known step-flow growth process (*31*, *32*) which occurs in many examples of crystal growth and serves as a foundation for continuum models of nanoparticle shape development (e.g., kinetic Wulff construction) and modern thin-film fabrication techniques (e.g., molecular beam epitaxy) (*23*, *32*).

To determine the generality of these observations, single-crystalline rhombic dodecahedron (RD) nanocrystals were etched under similar conditions (Fig. 3, G to L, and movies S27 to S30). Indeed, the elongated hexagonal projection of the RD is observed to transition through a THH intermediate (viewed edge-on as a result of the ⟨110⟩ zone axis) before being oxidized completely (Fig. 3, G and H). Although the experimental results show a {310} THH as the final kinetic product, simulations show a {210} THH (Fig. 3, I and J; fig. S28; and movies S31 to S34), suggesting that additional factors that are not considered in simulations (e.g., ligand binding to the larger {100} terrace area of {310} facets) (Fig. 4, C and D) may be important in dictating the precise facet morphology. (A similar discrepancy between the experiment and simulations for tip-selective nanorod etching supports the idea that ligand binding can modulate relative facet stability; see above, fig. S15, and movie S6.) Nonetheless, the qualitative observation of a period of transient metastability of a THH intermediate is confirmed and can be quantified through similar kinetic Wulff construction and time-domain contour plot analysis techniques (Fig. 3, K and L, and figs. S23 to S26). The appearance of THH intermediates is also observed from a rhombic dodecahedron and

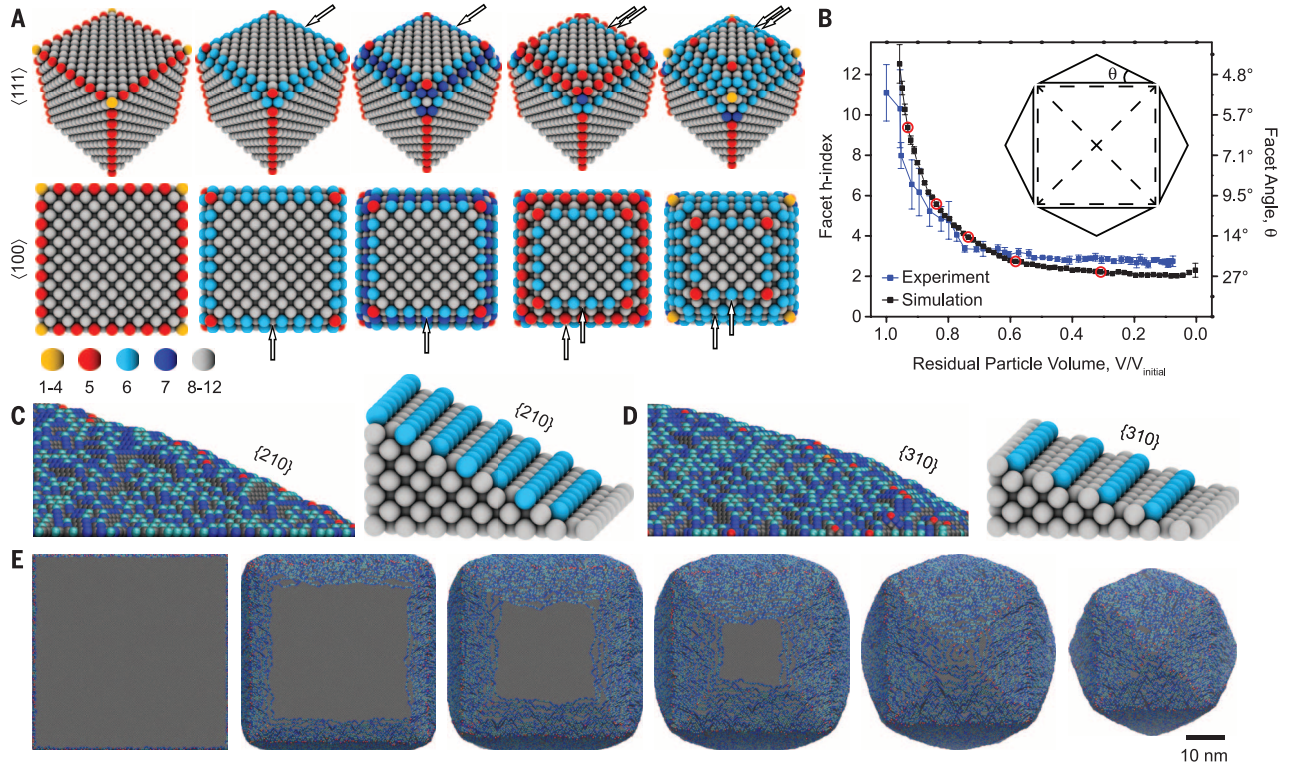

Fig. 4. Coordination number and step-recession–based formation mechanism of intermediate nanocrystals. (**A**) Idealized etching of a cubic nanocrystal shown from two crystallographic perspectives wherein atoms with coordination number (n) ≤ 6 are deterministically removed at each step (movie S26). Arrows denote the presence of {100} terraces that recede via removal of atoms at their step edges. Color-coded legend for n is shown at bottom left. (**B**) Time evolution of the vicinal facet effective h-index via measurement of the facet angle in both experiment and simulation (movies S17 and S19). Red circles correspond to the snapshots in (E). (**C** and **D**) Simulation snapshot (left) and perfect model facet (right) of {210} (C) and {310} (D) facets. (**E**) Simulation snapshots of the progression of a cube to a nonequilibrium THH with atoms color-coded according to coordination number (movie S20).

cube pair, etched in the same field of view under identical conditions (movie S35).

Our results suggest that the formation of a THH nanocrystal is a general property of fcc metals under a broad range of conditions that favor kinetic products. This may explain the observation that the synthetic nanocrystal literature contains a preponderance of reports of structures bounded by {hk0} rather than other, ostensibly equally likely, {hkl} facets (*26*, *27*). Additional nanocrystal shapes exhibited driving-force–dependent near-equilibrium and nonequilibrium transformation pathways, highlighting the generality of the observations described above (fig. S29 and movies S36 to S39).

In the chemistry of atoms and molecules, the study of reactive intermediates is key to understanding molecular reaction mechanisms, and new tools for observing such intermediates are constantly sought. An analogy is often made between nanocrystals and artificial atoms and molecules. Liquid cell TEM provides for observation and mechanistic understanding of transient intermediates in the formation of nanostructures at the relevant time and length scales. This will add to our rapidly developing ability to create and control artificial nanoscale building blocks with high precision.

REFERENCES AND NOTES

1. H. Zheng *et al.*, *Science* **324**, 1309–1312 (2009).
2. D. H. Son, S. M. Hughes, Y. Yin, A. P. Alivisatos, *Science* **306**, 1009–1012 (2004).
3. Y. Sun, Y. Xia, *Science* **298**, 2176–2179 (2002).
4. S. H. Tolbert, A. P. Alivisatos, *Science* **265**, 373–376 (1994).
5. P. Buffat, J. P. Borel, *Phys. Rev. A* **13**, 2287–2298 (1976).
6. M. J. Mulvihill, X. Y. Ling, J. Henzie, P. Yang, *J. Am. Chem. Soc.* **132**, 268–274 (2010).
7. M. N. O'Brien, M. R. Jones, K. A. Brown, C. A. Mirkin, *J. Am. Chem. Soc.* **136**, 7603–7606 (2014).
8. M. J. Williamson, R. M. Tromp, P. M. Vereecken, R. Hull, F. M. Ross, *Nat. Mater.* **2**, 532–536 (2003).
9. N. de Jonge, F. M. Ross, *Nat. Nanotechnol.* **6**, 695–704 (2011).
10. D. Li *et al.*, *Science* **336**, 1014–1018 (2012).
11. E. Sutter *et al.*, *Nat. Commun.* **5**, 4946 (2014).
12. Q. Chen *et al.*, *ACS Cent. Sci.* **1**, 33–39 (2015).
13. J. Wu *et al.*, *Nano Lett.* **15**, 2711–2715 (2015).
14. F. M. Ross, *Science* **350**, aaa9886 (2015).
15. J. M. Yuk *et al.*, *Science* **336**, 61–64 (2012).
16. J. Park *et al.*, *Science* **349**, 290–295 (2015).
17. T. J. Woehl, J. E. Evans, I. Arslan, W. D. Ristenpart, N. D. Browning, *ACS Nano* **6**, 8599–8610 (2012).
18. H.-G. Liao *et al.*, *Science* **345**, 916–919 (2014).
19. N. M. Schneider *et al.*, *J. Phys. Chem. C* **118**, 22373–22382 (2014).
20. Y. Xia, X. Xia, H.-C. Peng, *J. Am. Chem. Soc.* **137**, 7947–7966 (2015).
21. C.-K. Tsung *et al.*, *J. Am. Chem. Soc.* **128**, 5352–5353 (2006).
22. D. Alpay, L. Peng, L. D. Marks, *J. Phys. Chem. C* **119**, 21018–21023 (2015).
23. L. D. Marks, L. Peng, *J. Phys. Condens. Matter* **28**, 053001 (2016).
24. Z. Nie *et al.*, *Nat. Mater.* **6**, 609–614 (2007).
25. B. Goris *et al.*, *Nat. Mater.* **11**, 930–935 (2012).
26. X. Ye *et al.*, *Nano Lett.* **13**, 2163–2171 (2013).
27. M. L. Personick, M. R. Langille, J. Zhang, C. A. Mirkin, *Nano Lett.* **11**, 3394–3398 (2011).
28. M. Liu, Y. Zheng, L. Zhang, L. Guo, Y. Xia, *J. Am. Chem. Soc.* **135**, 11752–11755 (2013).
29. A. Feltz, U. Memmert, R. J. Behm, *Chem. Phys. Lett.* **192**, 271–276 (1992).
30. C. Y. Nakakura, E. I. Altman, *J. Vac. Sci. Technol. A* **15**, 2359–2368 (1997).
31. W. K. Burton, N. Cabrera, F. C. Frank, *Philos. Trans. R. Soc. London A* **243**, 299–358 (1951).
32. J. Krug, in *Multiscale Modeling in Epitaxial Growth*, A. Voigt, Ed. (Birkhäuser Basel, Basel, 2005), pp. 69–95.

ACKNOWLEDGMENTS

This work was supported in part by the King Abdulaziz City for Science and Technology (KACST), Kingdom of Saudi Arabia, which provided for nanocrystal synthesis; the Defense Threat Reduction Agency (DTRA) under award HDTRA1-13-1-0035, which provided for nanocrystal etching, postdoctoral support, and TEM instrumentation; the NSF-BSF International Collaboration in Chemistry program, NSF grant CHE-1416161 and BSF grant 2013/604, which provided for computational resources; and the Director, Office of Science, Office of Basic Energy Sciences, Materials Sciences and Engineering Division of the U.S. Department of Energy under contract DE-AC02-05CH11231 within the sp2-bonded Materials Program (KC2207), which provided for graphene growth, cell fabrication, and student support. This work made use of the Molecular Foundry, Lawrence Berkeley National Laboratory, which is supported by the U.S. Department of Energy under contract DE-AC02-05CH11231. Q.C. was supported by a Miller fellowship from Miller Institute for Basic Research in Science at UC Berkeley. G.M.R. acknowledges the NSF for a Graduate Research Fellowship. M.R.J. acknowledges the Arnold and Mabel Beckman Foundation for a postdoctoral fellowship.

SUPPLEMENTARY MATERIALS

www.sciencemag.org/content/354/6314/874/suppl/DC1
Materials and Methods
Figs. S1 to S36
Movies S1 to S43
References (*33*–*54*)

27 June 2016; accepted 14 October 2016
10.1126/science.aah4434

Science

Single-particle mapping of nonequilibrium nanocrystal transformations

Xingchen Ye, Matthew R. Jones, Layne B. Frechette, Qian Chen, Alexander S. Powers, Peter Ercius, Gabriel Dunn, Grant M. Rotskoff, Son C. Nguyen, Vivekananda P. Adiga, Alex Zettl, Eran Rabani, Phillip L. Geissler and A. Paul Alivisatos

Science **354** (6314), 874-877.
DOI: 10.1126/science.aah4434

Watching it all fall apart

The control of the shape and size of metal nanoparticles can be very sensitive to the growth conditions of the particles. Ye *et al.* studied the reverse process: They tracked the dissolution of gold nanoparticles in a redox environment inside a liquid cell within an electron microscope, controlling the particle dissolution with the electron beam. Tracking short-lived particle shapes revealed structures of greater or lesser stability. The findings suggest kinetic routes to particle sizes and shapes that would otherwise be difficult to generate.

Science, this issue p. 874